ACS APPLIED MATERIALS & INTERFACES

www.acsami.org

Research Article

Insight into the Activity and Selectivity of Nanostructured Copper Titanates during Electrochemical Conversion of CO_2 at Neutral pH via In Situ X-ray Absorption Spectroscopy

Matthew J. Lawrence, Veronica Celorrio,* Elizabeth Sargeant, Haoliang Huang, Joaquín Rodríguez-López, Yuanmin Zhu, Meng Gu, Andrea E. Russell, and Paramaconi Rodriguez*

Cite This: *ACS Appl. Mater. Interfaces* 2022, 14, 2742−2753

Read Online

ACCESS | Metrics & More | Article Recommendations | Supporting Information

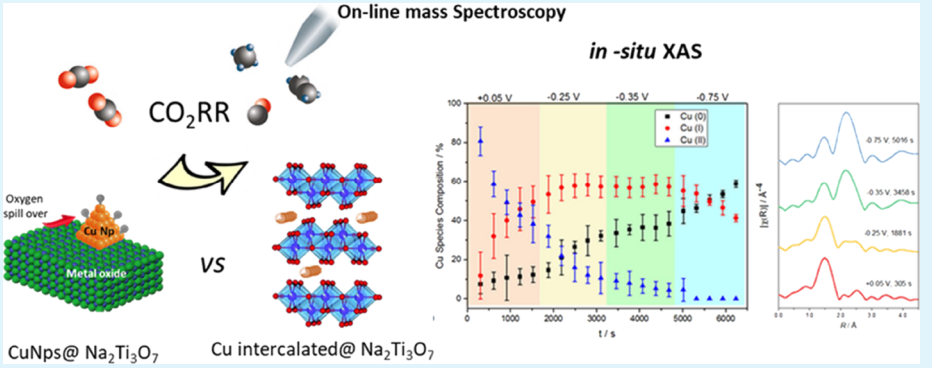

ABSTRACT: The electrochemical conversion of carbon dioxide (CO_2) to useful chemical fuels is a promising route toward the achievement of carbon neutral and carbon negative energy technologies. Copper (Cu)- and Cu oxide-derived surfaces are known to electrochemically convert CO_2 to high-value and energy-dense products. However, the nature and stability of oxidized Cu species under reaction conditions are the subject of much debate in the literature. Herein, we present the synthesis and characterization of copper-titanate nanocatalysts, with discrete Cu−O coordination environments, for the electrochemical CO_2 reduction reaction (CO_2RR). We employ real-time in situ X-ray absorption spectroscopy (XAS) to monitor Cu species under neutral-pH CO_2RR conditions. Combination of voltammetry and on-line electrochemical mass spectrometry with XAS results demonstrates that the titanate motif promotes the retention of oxidized Cu species under reducing conditions for extended periods, without itself possessing any CO_2RR activity. Additionally, we demonstrate that the specific nature of the Cu−O environment and the size of the catalyst dictate the long-term stability of the oxidized Cu species and, subsequently, the product selectivity.

KEYWORDS: *CO_2 reduction reaction (CO2RR), metal intercalation, layered structures, electrochemistry, copper catalyst, in situ XAS*

1. INTRODUCTION

The impacts of climate change and global warming have become a topical subject in both the political and scientific landscapes in recent times. The significant increase in anthropogenic carbon dioxide (CO_2) in the atmosphere through the widespread use of fossil fuels to meet the ever-increasing global demand and consumption of energy is of great concern.[1] The capture and recycling of atmospheric CO_2 is a promising pathway to address this global challenge.[2,3] In particular, the electrochemical conversion of CO_2 to useful, value-added chemicals is the subject of significant research effort because this avenue affords an opportunity to take advantage of electrical energy generated by renewable sources such as wind, water, and solar.[3−7]

The specific chemical and physical properties of the catalyst play a significant role in the electrochemical CO_2 reduction reaction (CO_2RR). Among all monometallic catalysts, copper- and copper oxide-derived surfaces are the most active catalysts that can electrochemically convert CO_2 to high-value and energy-dense C2 and C3 products.[8] Previous studies have demonstrated that surface geometry,[9,10] oxidation state,[11,12] particle size,[13,14] morphology,[15−17] and electrolyte composition[18,19] impact the selectivity and efficiency of the CO_2RR.

One of the most controversial aspects when studying the selectivity of the copper catalyst is the presence of surface and subsurface oxides.[20−23] However, while some reports suggest that copper oxides, at the surface or subsurface, are stable at the

Received: October 11, 2021
Accepted: December 15, 2021
Published: January 4, 2022

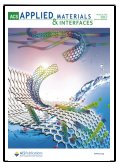

potentials where the CO_2RR takes place and their presence results in changes in the product selectivity, other researchers claim that the copper oxide derivatives fully reduce to copper during the CO_2RR and that it is the change of the surface structure which defines the changes in the product selectivity.[24] We recently proposed that the presence of surface oxides electrochemically generated via potential pulses results in changes in the product selectivity and the formation of oxygenated products.[22] Further quasi in situ studies by Roldan-Cuenya's group confirmed that the change in selectivity is associated with both changes in the surface structure and the presence of Cu(I) species.[12] Even though electrochemical potential pulses are, from the fundamental point of view, suitable to generate Cu(I) species and thus change the selectivity, the application of the method in CO_2 electrolysers is not trivial. Therefore, strategies to supply and retain oxygen on the copper catalyst will be necessary for the implementation of the CO_2RR.

Herein, we present the synthesis of a series of Cu-containing $Na_2Ti_3O_7$ (NTO) catalysts for the CO_2RR in a neutral aqueous phosphate electrolyte. The titanate motif was shown to be electrochemically stable under CO_2RR conditions and facilitates strong adsorption and chemisorption of CO_2 and CO_3^{2-}.[25] Thus, two distinct Cu titanates were prepared for this investigation: Cu-intercalated NTO (Cu:NTO) and CuO nanoparticles mixed with NTO (CuO@NTO). The nanoparticles were prepared via cathodic corrosion,[26] which enables the single-step preparation of oxide nanoparticles dispersed in aqueous solution that can be directly used as a catalyst without the need for additional chemical cleaning or calcination steps.[27,28] The catalytic activity and selectivity for the CO_2RR were evaluated for all the metal oxide catalysts used. In situ X-ray absorption spectroscopy (XAS) was used to determine the oxidation state and local coordination environment of the copper in Cu:NTO and CuO@NTO nanoparticles under the relevant CO_2RR conditions and thus, to establish a relationship between these parameters and the product selectivity determined by on-line electrochemical mass spectrometry (OLEMS) and NMR.

2. EXPERIMENTAL SECTION

2.1. Cathodic Corrosion Synthesis. A two-electrode configuration was employed for cathodic corrosion synthesis, as described previously, using LabVIEW/National Instruments hardware and a homebuilt power amplifier.[26,27,29,30] NTO and Cu:NTO nanowires were prepared by applying a square waveform oscillating between 0 and −10 V at 100 Hz across the working electrode (WE) (Ti wire of 0.25 mm diameter and $Cu_{19}Ti_{81}$ alloy, respectively) and a high-surface area Pt flag used as a counter electrode (CE), submerged in 10 M NaOH (Merck, ≥99%) solution.[26] The $Cu_{19}Ti_{81}$ alloy was prepared via suspended droplet alloying[31,32] (see the Supporting Information for experimental details). CuO nanoparticles were prepared by applying a square waveform oscillating between +4 and −4 V at 100 Hz across the working electrode (Cu wire of 0.41 mm) in 90% saturated $CaCl_2$ (Merck, anhydrous ≥93%).

The suspensions of nanoparticles were separated by repeated centrifugation at 4500 rpm and decanting of the supernatant until neutral pH was obtained. Catalysts were left suspended in Milli-Q water (PURELAB Ultra, 18.2 MΩ cm) prior to physical and electrochemical investigations.

To normalize the catalytic activity per mass, the clean samples were dried at 75 °C and weighed. CuO@NTO was prepared by adding 10% by weight of the CuO to a known mass of NTO nanowires to produce the 10 wt % CuO@NTO catalyst.

2.2. Physical Characterization. The nanomaterials were characterized by X-ray diffraction (XRD), scanning electron microscopy (SEM), and high-resolution transmission electron microscopy (HRTEM). Details of the instrumentation and methodology are described in the Supporting Information.

2.3. Electrochemical Characterization. A standard three-electrode configuration was employed for electrochemical measurements. The cyclic voltammetry (CV) curves were measured under mass transport conditions using a rotating disk electrode (RDE). Use of the RDE enabled the removal of surface-generated species during electrochemical investigation. A glassy carbon (GC) disk support assembled into a Teflon RDE holder was used as a support for the catalyst, and a high-surface area gold flag was used as a CE, with Ag/AgCl (3 M NaCl) used as the reference electrode (RE). All the graphs are presented with respect to the reversible hydrogen electrode (RHE) scale. All the measurements were performed in 0.1 M phosphate buffer solution (pH 8) produced from K_2HPO_4 (Acros Organics, >98%) and KH_2PO_4 (Sigma, ≥99%). Further details of the electrode loading and preparation and electrochemical measurements are presented in Supporting Information.

2.4. Product Characterization. OLEMS was used to detect the gaseous products formed during the reaction. The reaction products at the electrode interface were collected with a small tip positioned close to the electrode. The tip is a 2 mm diameter porous Teflon cylinder (Porex with an average pore size of 5−10 μm and 45−55% porosity) in a Kel-F holder. The tip configuration was cleaned overnight in a 2 M NaOH solution (VWR, EMSURE) and rinsed five times with ultrapure warm water before use. A secondary electron multiplier voltage of 1390 V was used, except for hydrogen ($m/z = 2$) where a secondary electron multiplier voltage of 2100 V was used. The pressure was equilibrated for 1 h prior to each measurement. During each experiment, multi-ion mass detection as a function of time was used. This program implies a progressive measuring of the different channels with a maximum of six channel detections and a time difference of 50 ms between the detection on each channel. One of the channels was used to follow the changes in the total pressure, and the other five channels were used to measure the following fragments: $m/z = 1$, $m/z = 15$, $m/z = 18$, $m/z = 26$, and $m/z = 28$, corresponding to H_2, CH_4, H_2O, C_2H_4, and CO/N_2, respectively. To determine the quantitative distinction of CO (as a product), CO (as a fragment of CO_2), and N_2 during the reduction of CO_2, the calibration method described by Binninger et al. was implemented.[33] The methodology for the NMR characterization of the liquid products is described in the Supporting Information.

2.5. In Situ XAS Characterization. Catalyst inks were prepared by adding 100 mg catalyst to 100 mg Vulcan carbon, 200 mg Nafion, and 1.5 mL of milli-Q water. The resultant mixtures were dispersed by ultrasonication until homogeneous inks were obtained. Button electrodes were prepared by painting the catalyst ink onto a carbon paper support (PTFE treated Toray Carbon Paper, Alfa Aesar) to generate a catalyst loading of 0.75 mg Cu cm^{-2}. The painted electrodes were hydrated in milli-Q water under vacuum prior to assembling into the in situ XAS cell. Spectra referred to as 'dry' were recorded free of any electrolyte solution and without any applied potential. Several scans were collected and merged to produce the reported spectra.

All measurements were collected in situ at room temperature at the B18 beamline of Diamond Light Source (UK),[34] using our custom-designed electrochemical cells in a three-electrode configuration,[35] connected to a μAutolab Type III potentiostat. The painted button electrodes were used as the WE with a gold wire CE and RHE RE. Calibration of the monochromator was carried out using a Cu foil, and XAS spectra were recorded in fluorescence mode at the Cu K-edge (8979 eV). The data were analyzed using Athena and Artemis programs, which implement the FEFF6 and IFEFFIT codes.[36] No data merge was performed with the in situ *operando* XAS spectra measured. For each catalyst and electrochemical environment, a series of potentials were applied cathodically from +0.05 to −0.75 V vs RHE, in succession, before returning back to +0.05 V. Several spectra were recorded at each potential, and the assigned times presented are based on the time elapsed from the initial recording of the in situ XAS spectra at +0.05 V. For the CO_2-saturated measurements, only XANES spectra were recorded while scanning the monochromator in both directions to minimize the time between individual scans. The time resolution for the

https://doi.org/10.1021/acsami.1c19298
ACS Appl. Mater. Interfaces 2022, 14, 2742−2753

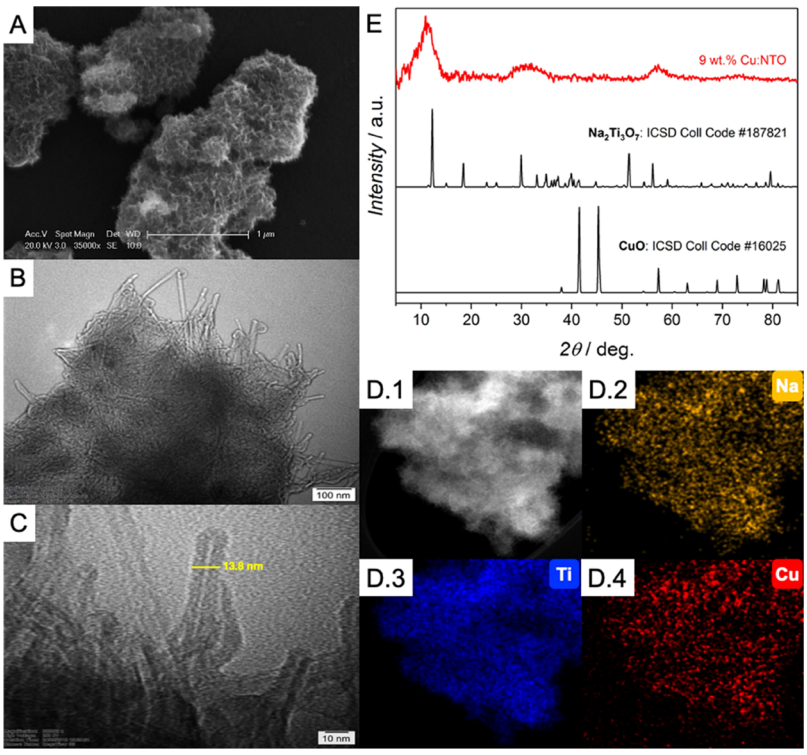

Figure 1. (A) SEM, (B) TEM, (C) HRTEM, and (D) HAADF and corresponding EDS elemental mapping images of 9 wt % Cu:NTO. (E) XRD pattern of 9 wt % Cu:NTO. ICSD database patterns for $Na_2Ti_3O_7$ [Coll Code 187821] and CuO [Coll Code 16025] are shown for comparison.

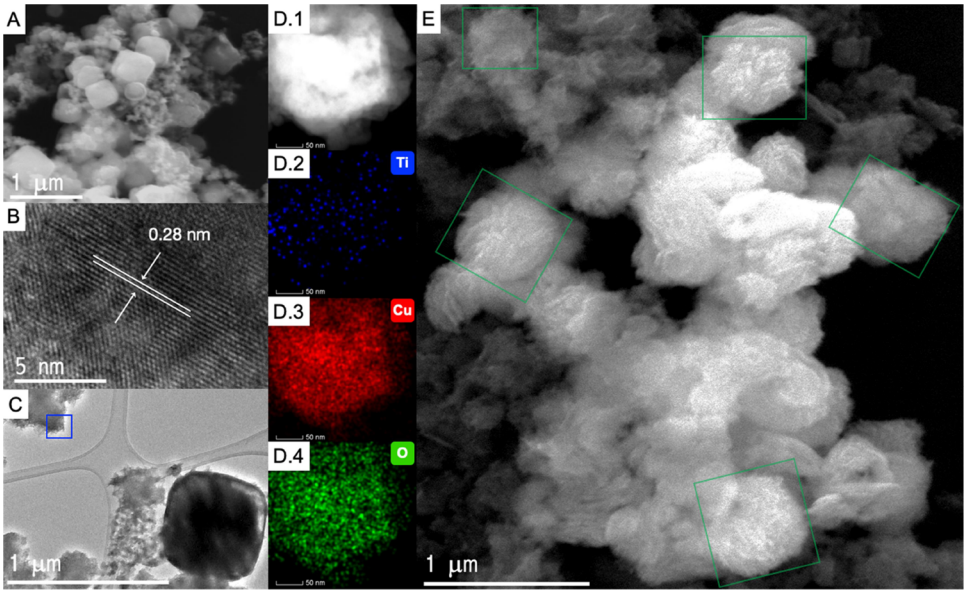

Figure 2. (A) Low-magnification SEM image and (B) HRTEM image of cubic CuO particles. (C) Low-magnification TEM image and (D) HAADF-STEM and corresponding EDS elemental mapping images of freshly prepared 10 wt % CuO@NTO. (E) Low-magnification SEM image of 10 wt % CuO@NTO after the catalyst was dispersed by ultrasonication in water for 30 min. Green squares highlight the presence of cube-like structures. The HRTEM image recorded at point indicated by blue square in (C) is presented in Figure S3.

measurements in the absence of CO_2 was 282 s, whereas the time resolution for measurements under relevant CO_2 conditions was 65 s. Details of data analysis are provided in the Supporting Information.

3. RESULTS AND DISCUSSION

3.1. Physicochemical Characterization of the Cu:NTO and CuO@NTO Catalysts. SEM and TEM images of 9 wt % Cu:NTO are presented in Figure 1. Discrete individual particles on the order of a few microns are observed, which consist of aggregated nanowires (Figure 1A). The TEM images (Figure 1B,C) provide further evidence of the intertwined nature of the nanowires that give rise to the larger particles. Particle size analysis indicated that the diameter of the 9 wt % Cu:NTO nanowires was 13.0 ± 2.6 nm (Figure S1A), in agreement with the previous work.[26] HAADF-STEM EDS elemental mapping was performed to probe the homogeneity of metals (Figure 1D).

https://doi.org/10.1021/acsami.1c19298
ACS Appl. Mater. Interfaces 2022, 14, 2742−2753

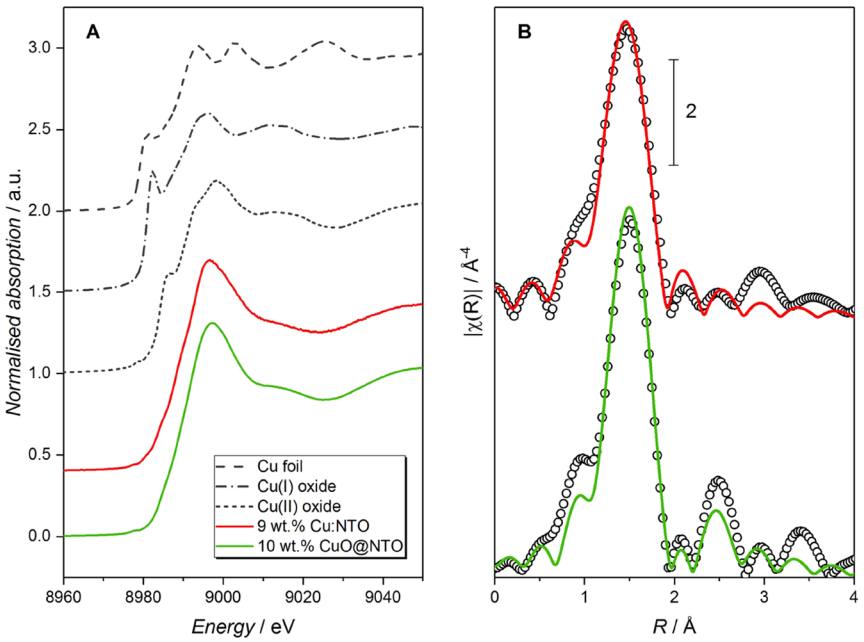

Figure 3. (A) Normalized Cu K-edge XANES spectra for the synthesized catalysts as well as reference materials. (B) FT (not phase corrected) of the k^3-weighted EXAFS data (empty circles) and fits (colored lines) of 9 wt % Cu:NTO (red) and 10 wt % CuO@NTO (green).

The homogeneous distribution of Na, Ti, and Cu throughout the particles probes the suitability of this methodology in the preparation of mixed metal oxide−layered nanomaterials. As can be seen in Figure 1E, the diffraction pattern of the intercalated Cu:NTO sample, there is a relative decrease in 2θ position for the $Na_2Ti_3O_7$ (100) peak around 11° indicative of the lattice expansion produced by the intercalation of hydrated Cu cations between the layers of TiO_6 octahedra, expanding the unit cell. Furthermore, peak broadening was observed, which is indicative of the low crystallinity of the nanostructured catalyst.

Electron micrographs of CuO and 10 wt % CuO@NTO produced via cathodic corrosion are presented in Figure 2. The CuO particles show cubic particles with an average diameter of 527 ± 73 nm (Figure S1B). HRTEM imaging of the cubic particles shows a distinct lattice spacing of 0.28 nm which corresponds to the (110) plane of CuO. The XRD pattern of the cubic CuO particles is presented in Figure S2b. The peaks at 2θ = 41.9, 45.1, 57.1, 63.1, 68.6, 72.8, 78.2, 79.0, and 80.9° correspond well with the (002) & ($11\bar{1}$), (111) & (200), ($20\bar{2}$), (020), (202),($11\bar{3}$), (022), ($31\bar{1}$), and (113) planes of CuO. The relatively narrow and intense diffraction peaks of the catalyst prepared in $CaCl_2$ are identical to the database pattern of monoclinic CuO and are indicative of the formation of highly crystalline CuO particles under the cathodic corrosion parameters employed. The diffraction pattern of 10 wt % CuO@NTO (Figure S2a) shows broad signals at 2θ = 10.2, 29.4, 33.2, and 57.1° that mirror the diffraction signals observed for the undoped NTO catalyst (Figure S2c). The peaks are in reasonable agreement with the corresponding (100), (110), (111), and (020) planes of crystalline $Na_2Ti_3O_7$ [ICSD Coll Code 187821]. The increased d-spacing of the NTO (100) indicated by the shift in 2θ is generated by the presence of hydrating water molecules within the titanate layers because of the low temperature used during the cathodic corrosion for the synthesis of layered titanate nanowires in an aqueous environment.[37] Additional low intensity peaks can be observed at 2θ = 41.9 and 45.1°, which correspond to the (002)/($11\bar{1}$) and (111)/(200) planes of crystalline CuO, respectively.

Upon mixing NTO and the CuO nanocubes, the presence of both the cubic CuO particles and the aggregated NTO nanowires as separate phases was observed for 10 wt % CuO@NTO (Figure 2C). Higher magnification TEM images show the presence of the aggregated nanowires (Figure S3). HAADF-EDS elemental mapping characterization of a CuO particle from the freshly prepared CuO@NTO catalyst demonstrates a cubic Cu−O matrix but also shows the presence of the Ti phase on the periphery. Following dispersion of the catalyst via ultrasonication, SEM characterization suggested that the presence of NTO at the surface of the Cu−O matrices had increased (Figure 2E).

Figure 3A presents the normalized XANES spectra of Cu foil, Cu(I), and Cu(II) standard oxide compounds in addition to the 'dry' 9 wt % Cu:NTO and 10 wt % CuO@NTO electrodes (prior to flooding the cell with electrolytes).

Comparison against the Cu foil and standard oxide compound references suggests that the Cu present in both 9 wt % Cu:NTO and 10 wt % CuO@NTO exists in a +2 oxidation state (first-derivative plot can be found in Figure S4A). The absorption edge energies, defined as the maximum of the first derivative, were 8993 and 8991 eV, respectively. The intense white line peaks at 8996 and 8997 eV, respectively, are attributed to the 1s → 4p (continuum) transition.[38] A very weak pre-edge feature at 8977 eV is observable for both catalysts, which is a characteristic of cupric Cu(II) d^9 compounds, generated by the quadrupole-allowed 1s → 3d transition.[38,39] The combination of these XANES features with the significantly reduced intensity of the 1s → $4p_z$ shakedown shoulder peak at 8986 eV is indicative of the presence of hydrated Cu^{2+} sites.[38,40]

Linear combination fit (LCF) analysis has been demonstrated as an effective means of elucidating the respective contributions of the various Cu species to measured XAS spectra.[41−43] Recently, it was demonstrated that the Cu oxidation state elucidated by the LCF of XANES spectra is within 3−4% accuracy.[44] The results for the 'dry' electrodes of 9 wt % Cu:NTO and 10 wt % CuO@NTO indicate a +2 Cu oxidation state (Table S1), in agreement with our XANES analysis.

https://doi.org/10.1021/acsami.1c19298
ACS Appl. Mater. Interfaces 2022, 14, 2742−2753

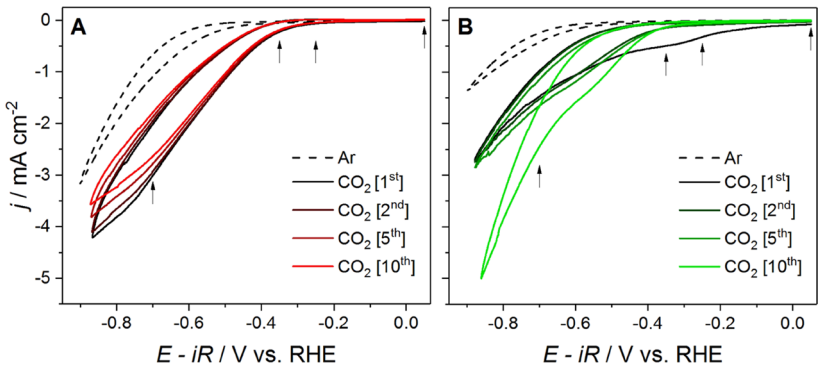

Figure 4. Cyclic voltammograms of (A) 9 wt % Cu:NTO and (B) 10 wt % CuO@NTO in Ar-saturated 0.1 M K_2HPO_4/KH_2PO_4 buffer solution (pH = 8) [dashed lines] and selected successive cyclic voltammograms in CO_2-saturated 0.1 M K_2HPO_4/KH_2PO_4 buffer solution (pH = 6.5); ν = 50 mV s^{-1} and rotation rate ω = 1200 rpm for all measurements. Arrows are indicators of the applied potentials utilized during in situ XAS measurements (see Section 3.3).

Figure 3B shows the comparison between the Fourier transforms (FTs) of the experimental EXAFS spectra (empty circles) and the best-fit simulations (colored lines) for 9 wt % Cu:NTO and 10 wt % CuO@NTO (k-space data are presented in Figure S4B). The first coordination shell peak at around 1.4 Å is observed for both catalysts, corresponding to the Cu−O scattering pair. A second coordination shell peak was only observed for 10 wt % CuO@NTO at ≈2.5 Å, corresponding to the Cu-Cu^{Metal} scattering pair. The best-fit parameters are summarized in Table S2.

3.2. Electrochemical Characterization of Cu:NTO and CuO@NTO Catalysts and Assessment of the Catalytic Activity toward the CO_2RR. Figure 4 shows the cyclic voltammograms of the 9 wt % Cu:NTO and 10 wt % CuO@NTO in a 0.1 M K_2HPO_4/KH_2PO_4 buffer solution in the absence and presence of CO_2. For the sake of comparison, the control cyclic voltammograms of undoped NTO recorded in an Ar-saturated phosphate buffer (pH = 8) are presented in Figure S5. The HER onset potential for the 9 wt % Cu:NTO appears at −0.487 V vs RHE, 20 mV more cathodic than the undoped NTO catalyst (Figure S6). The 10 wt % CuO@NTO sample showed an onset in the cathodic sweep at −0.580 vs RHE in the absence of CO_2 (Figure S6C). This could be attributed to two consecutive reactions; first, the reduction of the CuO nanoparticles to Cu followed by the HER. However, more insights into the reactions taking place in this potential region will be described later on the basis of the in situ XAS characterization. It is also important to notice that the current density for 9 wt % Cu:NTO is twice that of 10 wt % CuO@NTO at −0.9 V vs RHE under Ar-saturated conditions. At this potential, where only the HER is expected, the results indicate that the HER activity is significantly hindered by the interface of the NTO phase with CuO. In contrast, the presence of doped Cu^{2+} ions between titanate layers enhanced the HER activity (the measured current density) magnitude at −0.9 V relative to undoped NTO.

Prior to evaluating CO_2RR activity of the Cu-containing titanates, measurements were performed with pure NTO to understand the electrochemical behavior of the titanate phase in the presence of CO_2. It is important to note that upon saturation with CO_2 the pH of the 0.1 M buffer solution decreased from pH = 8 to pH = 6.5. Figure S5B shows the cyclic voltammograms of NTO in the CO_2-saturated phosphate buffer. Comparison of the current density profiles measured in the presence and absence of CO_2 indicates that NTO possesses negligible CO_2RR activity. The first cycle recorded in the CO_2-saturated electrolyte closely resembled that of the first 'blank' cycle (Figure S5A). The decrease in pH did not have an enhancing effect on the catalytic activity of the NTO toward the HER, when the reaction should have been more facile. Rather, a −33 mV shift in onset potential was determined (Figure S6D). Notably, in the presence of dissolved CO_2 and reduced pH, the anodic peak observed in the Ar-saturated voltammograms disappeared. The anodic peak observed in the voltammograms following a cathodic sweep is caused by the accumulation of charge (electrons) in the absence of an electrochemical reaction that subsequently discharges during the anodic scan. This could be attributed to the greater affinity for and stronger binding of CO_2 to the Ti surface sites. Additionally, two competing processes occur at nanoporous titanate semiconductor electrodes in aqueous electrolytes: catalytic and capacitive.[45] The anodic peak is not visible in the return sweep if an electrochemical reaction occurs because of the consumption of the electrons. Therefore, our results suggest that in Ar-saturated phosphate, the HER does not occur at the NTO catalyst in the potential range applied, rather, the catalyst acts as a capacitor. In the presence of CO_2, electrons are consumed for the CO_2RR, albeit with low current density measured, suggesting that the undoped catalyst is not active for the CO_2RR.

In the presence of dissolved CO_2, an anodic shift in the reduction onset potential of +156 mV relative to the Ar-saturated measurements was observed (Figure S6E). In addition, the overall current density measured in the applied potential range increased. Through subsequent cycles, the activity of the CO_2RR decreases, i.e., the peak current density decreased and the onset potential remained constant.

To investigate the impact of the decrease in pH induced by the dissolution of CO_2 in the electrolyte, H_3PO_4 was added to the 0.1 M K_2HPO_4 / KH_2PO_4 buffer solution until pH = 6 was reached. The voltammograms are shown in Figure S7. The current density of the voltammogram at pH = 6 of the sample 9 wt % Cu:NTO did not vary significantly from that obtained at pH = 8. These results confirmed that the relative shift in the onset potential observed was not wrought simply by the change in pH, but rather, it was a direct result of the presence of dissolved CO_2; thus, the onset potential observed was due to the CO_2RR on this catalyst.

The voltammetric profile of 10 wt % CuO@NTO in CO_2-saturated phosphate buffer solution is presented in Figure 4B. In the initial scan between +0.05 and −0.2 V vs RHE, the cathodic current density was significantly larger than the current density

https://doi.org/10.1021/acsami.1c19298
ACS Appl. Mater. Interfaces 2022, 14, 2742−2753

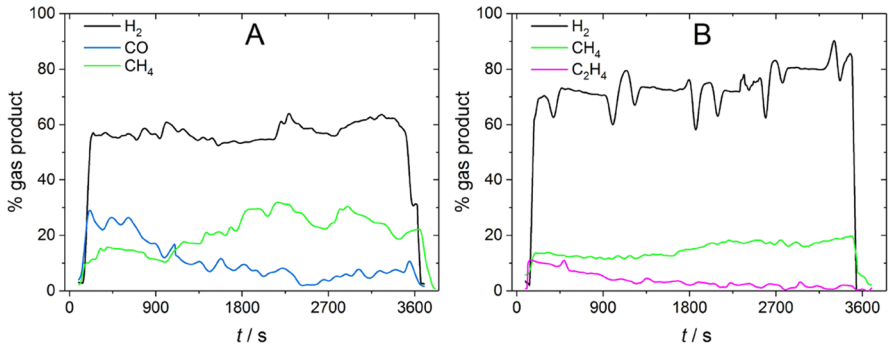

Figure 5. Product characterization of gases produced during the CO_2RR at −0.8 V vs RHE on (A) 9 wt % Cu:NTO and (B) 10 wt % CuO@NTO in CO_2-saturated 0.1 M K_2HPO_4/KH_2PO_4 buffer solution (pH 6.5).

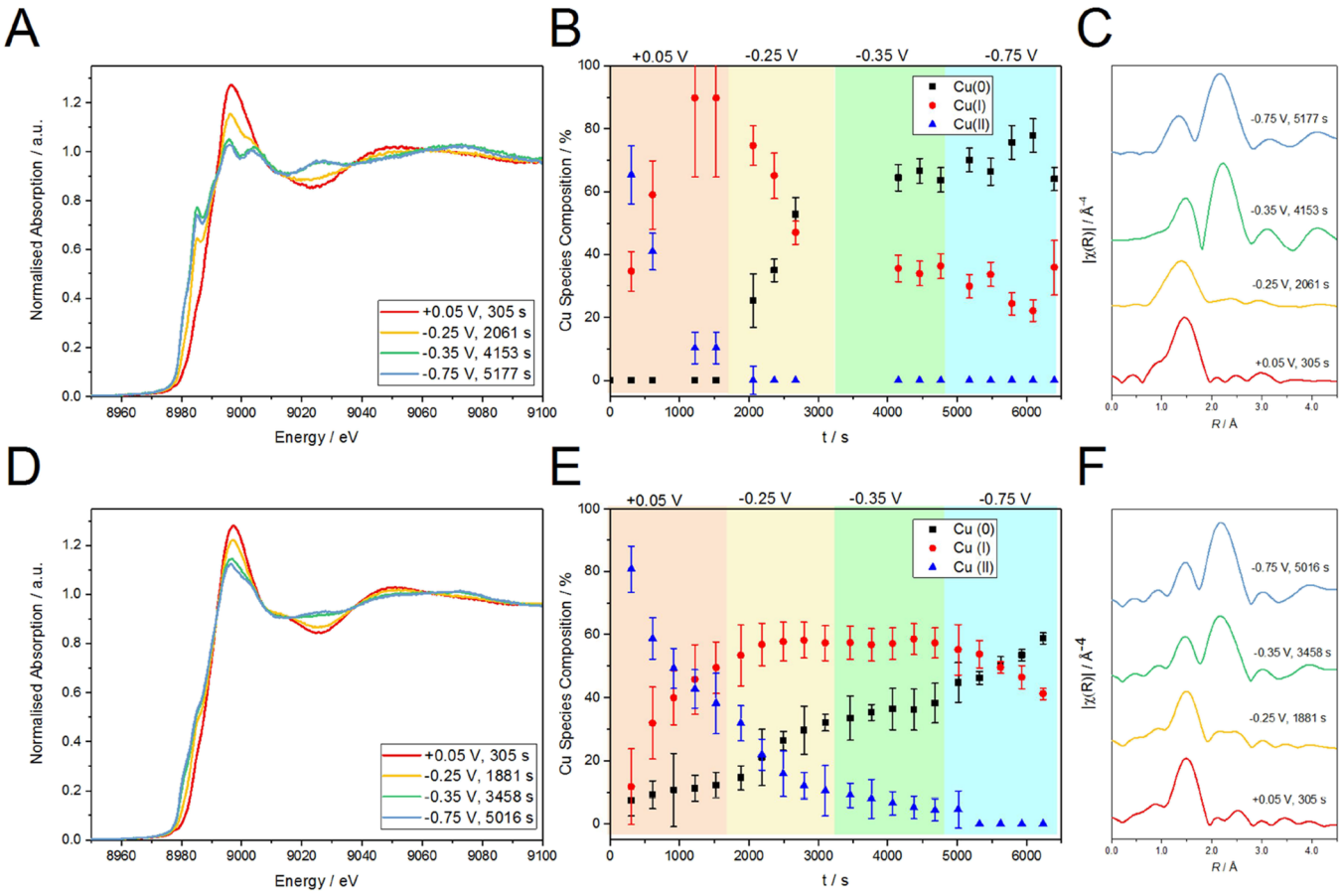

Figure 6. In situ XAS characterization of 9 wt % Cu:NTO and 10 wt % CuO@NTO in Ar-saturated 0.1 M K_2HPO_4/KH_2PO_4 solution (pH 8) at different applied potentials. Representative in situ XAS spectra of (A) 9 wt % Cu:NTO and (D) 10 wt % CuO@NTO. LCF determination of Cu species composition from in situ XANES spectra for (B) 9 wt % Cu:NTO and (E) 10 wt % CuO@NTO. Representative EXAFS Fourier Transforms (not phase corrected) of (C) 9 wt % Cu:NTO and (F) 10 wt % CuO@NTO.

measured in the absence of CO_2. The voltammogram also shows a wave between −0.2 and −0.4 V only observed during the first cycle and was, therefore, attributed to a surface reconstruction. The changing Cu coordination environment of the CuO-derived catalyst upon cycling had a significant impact on CO_2RR activity. Notably, for the first six cycles, the peak current density increased gradually followed by a significant increase of the catalytic activity observed during the seventh cycle that resulted in a near 2-fold increase in peak current density measured at −0.9 V vs RHE. Contrasting this behavior with that of the 9 wt % Cu:NTO mixed phase catalyst where no change in the onset potential was observed for the duration of the 10 cycles indicates that the gradual enhancement in activity of the CuO-based catalyst may be attributed to a structural surface activation process that rendered increased intrinsic activity of the Cu sites. This observation is in agreement with the existing literature on the enhanced activity of oxide-derived Cu catalysts toward the CO_2RR because of the increase in surface roughness and under-coordinated sites by the electrochemical reduction of the Cu oxide catalysts, generating metallic Cu NPs.[46−48] Further analysis of the chemical nature of the Cu catalyst will be presented in Section 3.3.

To summarize, we have established that the electrocatalytic activity observed for the two Cu-containing titanate nanostruc-

https://doi.org/10.1021/acsami.1c19298
ACS Appl. Mater. Interfaces 2022, 14, 2742−2753

tures toward the CO_2RR in near-neutral phosphate buffer solution is not simply a function of the chemical composition of the catalysts. The physical and structural properties contribute significantly to the observed activity. Consequently, it is the specific chemical and structural nature of each catalyst generated during CO_2RR electrolysis that produces the greatest impact on the activity and product selectivity.

To gain further insights regarding the reactivity of the two Cu-containing titanate nanostructures toward the CO_2RR, long-term electrolysis reactions were performed while following the gas products via OLEMS. Figure 5 shows the distribution of gaseous products for the CO_2RR on 9 wt % Cu:NTO (A) and 10 wt % CuO@NTO (B) during 1-h electrolysis at −0.8 V vs RHE. In the case of 9 wt % Cu:NTO, the formation of H_2 (m/z = 2) accounts for the majority of gas products evolved during the electrolysis (50−65%). The formation of CO (m/z = 28) and CH_4 (m/z = 16) was also detected during the electrolysis. An inverse relationship was observed between the fractions of CO and CH_4 as the reaction progressed. The decrease in CO (a $2e^-$ product) was accompanied by a near-equivalent increase in the concentration of CH_4 (an $8e^-$ product). The change in gaseous product distribution is an indication of changes in the chemical state of the catalyst during the CO_2RR electrolysis. Further analysis will be discussed in Section 3.3 using in situ EXAFS.

In comparison, a greater percentage of H_2 was detected during the CO_2RR electrolysis on 10 wt % CuO@NTO than for the Cu:NTO, gradually increasing to >80% after 1 h. The percentage of CH_4 formed was similar to that observed for 9 wt % Cu:NTO and also increased gradually over the duration of the electrolysis. However, two significant differences were observed. A C_2 product, C_2H_4 (m/z = 26), was initially detected in low abundance which subsequently decreased overtime as the CH_4 increased and no CO was detected. The variation in products once again suggests that changes in the structure or chemical nature of the catalyst occur, favoring the formation of CH_4 over C_2H_4 for the CuO-derived catalyst or CO for the Cu:NTO mixed catalyst.

Liquid products were probed by ^1H NMR; however, in contrast to previous results on bulk and other copper nanocatalysts,[15,22,46,49,50] no appreciable quantities of liquid products were detected after 1 h of CO_2RR electrolysis for both catalysts. This is probably related to the difference in particle size of our catalyst with respect to those reported in the literature and the differences between supported catalyst (this work) and unsupported catalyst in previous reports.

3.3. In Situ X-ray Absorption Spectroscopy (XAS) Characterization in the Absence of CO_2. To better understand the structural and chemical changes undergone by Cu in both 9 wt % Cu:NTO and 10 wt % CuO@NTO during the CO_2RR, in situ XAS measurements were performed under chronoamperometric conditions. First, and to be used as a comparison, data were collected in Ar-saturated 0.1 M phosphate buffer, at +0.05, −0.25, −0.35, and −0.75 V (as indicated in Figure 6).

Representative XANES spectra collected for 9 wt % Cu:NTO and 10 wt % CuO@NTO in Ar-saturated 0.1 M phosphate buffer at different potentials are shown in Figure 6A,D, respectively (the full data set is shown in Figure S8). For 9 wt % Cu:NTO, a decrease in the absorption edge energy and intensity of the white line peak was observed with increasing time under reducing conditions. The decrease in absorption edge energy is indicative of the reduction in the oxidation state of the analyte species. The accompanying emergence of a low intensity peak at 8984 eV is indicative of the bulk reduction of Cu(II) and presence of Cu(I) in the catalyst.[41] After recording spectra at +0.05 and −0.25 V (Figure S8A,B), the intense white line peak previously seen in the spectra of the 'dry' electrode had disappeared, and two distinguishable peaks at 8995 and 9004 eV, resembling the XANES peaks observed for metallic Cu, were observed. We observed minimal further changes to the XANES features at −0.35 V and at −0.75 V.

A similar decrease in white line peak intensity and a negative shift in the absorption edge energy were observed under increasingly reducing conditions on 10 wt % CuO@NTO. Likewise, the emergence of the peak at 8984−8985 eV was also observed. Similar to 9 wt % Cu:NTO, there were minimal changes to the XANES features observed at −0.35 V. However, direct qualitative comparison of the XANES spectra obtained at each applied potential demonstrates that the change in the Cu oxidation state was noticeably more gradual for 10 wt % CuO@NTO. The twin peaks at ca. 8995 and 9004 eV became distinguishable for CuO@NTO at −0.75 V, whereas for Cu:NTO they were distinguishable at −0.25 V. Furthermore, the peak at 8985 eV was still a small shoulder at −0.75 V for CuO@NTO but was fully defined at −0.25 V for Cu:NTO.

Changes in Cu(0)/Cu(I)/Cu(II) speciation with potential over time were followed by LCF (Figure 6B,E). Overall, the data show that Cu^{2+} sites in 9 wt % Cu:NTO and 10 wt % CuO@NTO are reduced at different rates, suggesting that the CuO-containing catalyst is chemically more robust, experiencing relatively more gradual Cu^{2+} reduction and a higher overall approximate Cu oxidation state following cathodic treatment. This was in agreement with the qualitative analysis of the XANES spectra. Our analysis also reveals that a significant fraction of Cu(I) is retained even under the most cathodic conditions, in agreement with previous studies.[51] A discussion about the reversibility of these processes can be found in the Supporting Information (Figure S9).

Figure 6C,F shows the comparison between the FTs of the EXAFS data at different potentials for 9 wt % Cu:NTO and 10 wt % CuO@NTO (full k^3 weighted data are shown in Figures S10 and S11, with best fit parameters presented in Tables S5 and S6). Generally, the EXAFS FTs for the two catalysts were similar in appearance. Under an applied potential of +0.05 V, a first coordination shell peak at around 1.4 Å can be observed for both catalysts, corresponding to Cu−O scattering.

The EXAFS fits for 9 wt % Cu:NTO identified the coexistence of octahedral ($Cu-O^{Oh}$, characteristic of Cu(II) species) and tetrahedral ($Cu-O^{Th}$, characteristic of Cu(I) species) Cu coordination environments at +0.05 V (Table S5). The calculated bond lengths for both environments slightly reduce with increasing time, suggestive of a reduction in overall Cu oxidation state. Indeed, the EXAFS fit of the FT of the first in situ XAS spectrum measured at −0.25 V indicates the presence of $Cu-Cu^{metal}$ scattering and the absence of $Cu-O^{Oh}$. This was accompanied by the emergence of a second shell coordination peak at ∼2.2 Å, corresponding to $Cu-Cu^{metal}$. However, the $Cu-O^{Th}$ scattering still contributes to the EXAFS FT at −0.25, −0.35, and −0.75 V vs RHE. This is demonstrated visually in the EXAFS FT by the persistence of the Cu−O peak at ∼1.4 Å (Figure 6C). These results agree with the Cu species composition determined via LCF fit analysis.

The coordination number (CN) of the $Cu-Cu^{metal}$ scattering increases under more negative applied potential, rising from 2.3 ± 1.0 at −0.25 V to 6.2 ± 0.6 at −0.75 V. Interestingly, the $Cu-O^{Th}$ CN increases at −0.25 V, the potential at which LCF

https://doi.org/10.1021/acsami.1c19298
ACS Appl. Mater. Interfaces 2022, 14, 2742−2753

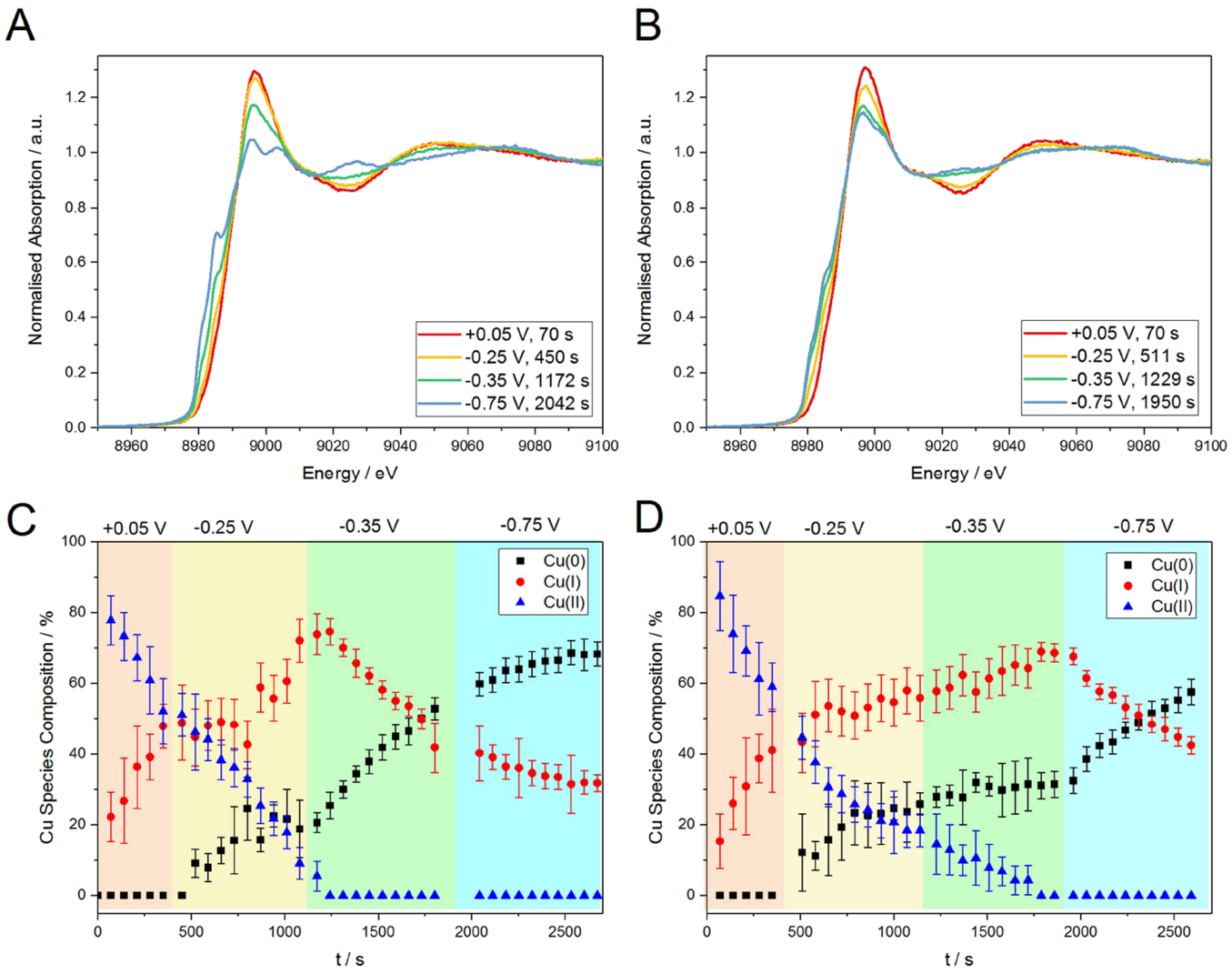

Figure 7. Representative in situ XANES spectra of (A) 9 wt % Cu:NTO and (B) 10 wt % CuO@NTO in CO_2-saturated 0.1 M K_2HPO_4/KH_2PO_4 solution (pH 6.5) under different applied potentials. (C, D) LCF determination of Cu species composition from (A) and (B), respectively.

analysis indicates that all Cu^{2+} is reduced, and there is a relatively high Cu(I) contribution in 9 wt % Cu:NTO. At more negative potentials, the Cu−O^{Th} CN decreases, but not significantly relative to the 'dry' catalyst and initial in situ measurement. Combined, these results suggest the formation of metallic Cu clusters with an increasing size at 9 wt % Cu:NTO following the degradation of Cu^{2+} octahedra under reducing conditions. The clustering would require mobility of the Cu atoms, which could perceivably be facilitated by the channels of the titanate layers. Further in situ XAS at the Ti K-edge would shed more light on the specific nature of the cluster formation process, but the lower energy of the Ti K-edge and absorption of water at those energies prevent the study. The EXAFS fit results did not suggest any contribution from Cu−O^{Oh} in the FT of 10 wt % CuO@NTO (Table S6), unlike 9 wt % Cu:NTO. Thus, we conclude that the Cu−O^{Oh} environment identified in 9 wt % Cu:NTO is characteristic of the single-atom Cu complexes doped in NTO, i.e., octahedral Cu complexes within the titanate layers.

With 10 wt % CuO@NTO, a low-intensity Cu−Cu coordination shell peak at ∼2.5 Å can also be observed that corresponds to the Cu−Cu^{metal} environment indicated by EXAFS fit of the 'dry' electrode. During the in situ measurements, the Cu−O^{Th} CN decreased with increasingly negative applied potential, whereas the Cu−Cu^{metal} CN increased. However, the Cu−O^{Th} contribution was present in all EXAFS fit results and indicated the presence of stable oxidized Cu species under reducing conditions. As above, the results obtained from the fitted EXAFS data are in good agreement with those determined by LCF.

3.4. In Situ XAS Characterization of the Cu Titanates under Relevant CO_2RR Conditions. Figure 7 presents representative in situ XANES spectra and LCF determination of Cu species composition for 9 wt % Cu:NTO and 10 wt % CuO@NTO in CO_2-saturated phosphate (the full set of XANES spectra is presented in Figure S12). Results of the LCF analysis, including the estimated Cu oxidation states, are tabulated in Tables S7 and S8, respectively.

The changes to the in situ XANES observed in the presence of CO_2 were similar to what was observed in the Ar-saturated electrolyte, i.e., as increasingly more negative potentials were applied, the edge energy decreased, a peak at 8984−8985 eV emerged, and the relative intensity of the white line decreased for both catalysts (Figure 7A,D). The distinguishable twin peaks at 8995 and 9004 eV were observed first for 9 wt % Cu:NTO at −0.35 V, whereas they were only observed at −0.75 V for 10 wt % CuO@NTO (Figure S12H). The overall XANES features did

https://doi.org/10.1021/acsami.1c19298
ACS Appl. Mater. Interfaces 2022, 14, 2742−2753

not change significantly any further even at more negative applied potentials for this catalyst (Figure S12D). The results again suggested that the reduction of Cu in 9 wt % Cu:NTO was more facile relative to 10 wt % CuO@NTO. LCF analysis further confirmed this (Figure 7C,D). The point at which metallic Cu species became the dominant species was at applied potentials of −0.35 and −0.75 V for 9 wt % Cu:NTO and 10 wt % CuO@NTO, respectively.

A similar approximate Cu oxidation state was suggested by LCF analysis of the in situ XANES spectra of 9 wt % Cu:NTO under both CO_2-saturated and CO_2-free conditions (Table S7), likewise, for 10 wt % CuO@NTO. Similar Cu oxidation states for each catalyst were obtained regardless of the duration of the measurements, which demonstrates that the applied potential imposes the greatest effect in the reduction of oxidized Cu species in 0.1 M K_2HPO_4/KH_2PO_4. An analogous observation was recently reported using 100 mM $KHCO_3$.[52] Our results agree with recent in situ and *operando* XAS studies that have also determined the presence of oxidized Cu species during and following the CO_2RR at nanostructured oxide-derived Cu catalysts.[11,44] However, our work reports a higher in situ Cu(II) composition than has been reported previously.

Although the Cu−O bond is thermodynamically unstable under reducing conditions, the stability of the Cu−O bond under CO_2RR conditions has been reported previously for both bulk and nanostructured Cu catalysts.[11,53−55] Such stability has been linked to changes of the electronic structure of Cu because of dopant materials,[56] alloying,[57,58] strain effects, strong metal support interactions,[59] or even spill-over of oxygen. Indeed, the synthetic method employed in production of the catalyst will also impact the stability of Cu−O. One possible factor for the observed enhanced stability of Cu−O in CuO@NTO is that the low-coordinated sites which are formed during the cathodic corrosion synthesis of the Cu particles bind more strongly to oxygen, helping to stabilize oxides during the reaction. Cathodic corrosion is a synthetic method that occurs far from equilibrium. Thus, strain is introduced to the surface by the cathodic corrosion mechanism, i.e., formation of Cu metallides, causing strong oxygen binding. Another possibility is that the high local pH could help us to stabilize Cu^+ by negatively shifting the overpotential for Cu_2O reduction. The exact mechanism is still being investigated via in situ experiment and theory.

The in situ XANES spectra measured in our work were obtained using a successive applied potential regime, increasing the magnitude of cathodic potential in stages to monitor the change in Cu oxidation state with time. Thus, although the total measurement time is comparable, the overall cathodic potential applied to the catalysts differs, and we have demonstrated that the magnitude of the applied cathodic potential has a significant impact on the nature of the Cu catalyst.

XAS techniques probe the bulk of the catalysts. Given the difference in the particle size between the Cu:NTO and CuO@NTO catalysts, the LCF analyses for Cu:NTO are more reflective of the chemical nature of the catalyst surface generated under reducing conditions in the phosphate electrolyte, whereas the core of the CuO nanocubes in CuO@NTO adds greater weighting to the LCF results than the catalyst surface. It must also be noted that the decrease in pH upon saturating the electrolyte with CO_2 accelerates the reduction of Cu species such that similar reduced Cu oxidation states can be obtained in significantly shorter timescales.

Under CO_2RR conditions, we focused on maximizing the time-resolution of the in situ XANES spectra, employing a narrower energy range for the measurements and an increased scan speed. Thus, accurate EXAFS fitting of the FTs of the in situ CO_2RR XANES spectra was not possible. However, given the similarities in the XANES features and LCF Cu species composition determined under CO_2RR conditions, we have drawn on the EXAFS fit results obtained in the absence of CO_2 to relate the structural changes to the electrochemical activity and product distributions discussed.

Relating the in situ CO_2-saturated XANES and EXAFS results with the OLEMS results provides insight into the roles of Cu species in the formation of the observed gaseous products. For the case of 9 wt % Cu:NTO, the XANES and EXAFS fit results suggest that the as-prepared catalyst possesses predominantly discrete $Cu-O^{Oh}$ that are electrochemically reduced and subsequently migrate and aggregate to form metallic Cu clusters over time under reducing conditions. Thus, the change in CO_2RR gaseous product distribution determined via OLEMS is a direct result of the nucleation and growth of metallic Cu species. At the beginning of the reduction process, when the metallic Cu species are beginning to form, the major gas product is CO and CH_4 is a minor gas product. As the metallic Cu clusters increase in population and size (as determined by EXAFS fit results), CH_4 becomes the major CO_2RR gas product. Our results are in agreement with Reske et al. who demonstrated that the dominant CO_2RR products were H_2 > CO > CH_4 for Cu nanocatalysts with sizes up to ≈20 nm.[14] Furthermore, the formation of metallic Cu clusters would decrease the availability of Cu active sites, resulting in a decrease in catalytic activity as we observed via cyclic voltammetry.

The EXAFS fit results for 10 wt % CuO@NTO indicate the formation of under-coordinated metallic Cu clusters under reducing conditions. The $Cu-O^{Th}$ CN of this catalyst is near-identical to that of 9 wt % Cu:NTO in their reduced forms. The significant difference compared to Cu:NTO was in the $Cu-Cu^{metal}$ CN. Furthermore, the formation of Cu clusters from 10 wt % CuO@NTO is effectively a reduction in the particle size and an increase in the specific surface area, the clusters seemingly forming from fragmentation of the large CuO cube-like structures. The possible formation of smaller Cu clusters that possess highly reactive under-coordinated sites provides an explanation for the enhanced catalytic activity observed via CV. With respect to the OLEMS results, it has been reported that oxide-derived Cu CO_2RR catalysts generated from the reduction of nanocubes, which possess a high ratio of Cu(100) sites, form little to no CH_4 with increased efficiency toward C_2H_4 formation.[60−62] Thus, our results therefore suggest that 10 wt % CuO@NTO possesses a low ratio of Cu(100) sites prior to reduction and formation of metallic clusters under reaction conditions.

4. CONCLUSIONS

We have demonstrated the versatility of the cathodic corrosion method in the preparation of nanostructured metal oxide electrocatalysts by the effective preparation of Cu(II) NTO catalysts with intrinsically different Cu coordination environments. Namely, we investigated the differences between discrete Cu complexes in 9 wt % Cu:NTO and a CuO lattice in 10 wt % CuO@NTO.

XRD characterization indicated the presence of CuO in the mixed phase catalyst. Electron microscopy demonstrated that interaction between the CuO and NTO forms a core-shell type structure in which CuO cubes are encompassed by the NTO nanowires. The absence of any diffraction pattern features

https://doi.org/10.1021/acsami.1c19298
ACS Appl. Mater. Interfaces 2022, 14, 2742−2753

corresponding to either metallic or oxidized Cu for 9 wt % Cu:NTO, combined with the homogeneous Cu distribution observed via HAADF-EDS, was indicative that the intercalated Cu did not form metallic or oxidic Cu clusters. This was confirmed via XANES analysis.

Electrochemical measurements in the absence of CO_2 demonstrated that the presence of intercalated Cu affords enhanced current density relative to undoped NTO, an enhancement not afforded by the CuO@NTO catalyst. CO_2RR activity was probed by CV and electrolysis, with gaseous products from the electrolysis characterized by OLEMS. We demonstrated that the NTO phase alone does not contribute to any observable CO_2RR activity, but rather that the NTO surface is poisoned, as evidenced by the progressive decrease in double layer capacitance through subsequent CV cycles in the presence of CO_2. The observed CO_2RR activity on 9 wt % Cu:NTO was therefore ascribed to the presence of Cu within the titanate layers, which, under reducing conditions, forms metallic Cu clusters with increasing size. OLEMS characterization identified that the gaseous products generated by the CO_2RR at −0.8 V vs RHE on 9 wt % Cu:NTO over 1 h were H_2, CO, and CH_4, with a shift in the initially observed CO:CH_4 ratio coinciding with an increase in cluster size. For 10 wt % CuO@NTO, the gaseous products identified were H_2, CH_4, and C_2H_4. A decrease in detected C_2H_4 and a subsequent increase in CH_4 concentration were ascribed to a decrease in the particle size, providing rationale for the increase in catalytic activity observed via CV. Generally, the reduction of the Cu^{2+} species was more gradual for the CuO-derived catalyst under CO_2RR conditions. LCF analysis of in situ XANES spectra recorded in the presence and absence of CO_2 indicated the stable presence of Cu(I) at −0.75 V vs RHE for both catalysts. Further in situ investigation regarding the specific role of NTO during CO_2RR electrolysis with the catalysts is required to enable elucidation of mechanistic pathways for the respective electrocatalysts.

■ ASSOCIATED CONTENT

Supporting Information

The Supporting Information is available free of charge at https://pubs.acs.org/doi/10.1021/acsami.1c19298.

Methodology; alloy preparation; HRTEM, size distribution and XRD of the nanomaterials; fit analysis results for in -situ XANES and EXAFS distances and fitting experiments parameters; in situ XANES spectra, and cyclic voltammograms (PDF)

■ AUTHOR INFORMATION

Corresponding Authors

Veronica Celorrio − *Diamond Light Source Ltd, Diamond House, Didcot OX11 0DE, U.K.;* orcid.org/0000-0002-2818-3844; Email: veronica.celorrio@diamond.ac.uk

Paramaconi Rodriguez − *School of Chemistry, University of Birmingham, Edgbaston, Birmingham B15 2TT, U.K.;* orcid.org/0000-0002-1517-0964; Email: p.b.rodriguez@bham.ac.uk

Authors

Matthew J. Lawrence − *School of Chemistry, University of Birmingham, Edgbaston, Birmingham B15 2TT, U.K.*

Elizabeth Sargeant − *School of Chemistry, University of Birmingham, Edgbaston, Birmingham B15 2TT, U.K.*

Haoliang Huang − *School of Chemistry, University of Southampton, Highfield, Southampton SO17 1BJ, U.K.*

Joaquín Rodríguez-López − *Department of Chemistry, University of Illinois Urbana−Champaign, Urbana, Illinois 61801, United States;* orcid.org/0000-0003-4346-4668

Yuanmin Zhu − *School of Materials Science and Engineering, Dongguan University of Technology, Dongguan 523808, China; Department of Materials Science and Engineering, Southern University of Science and Technology, Shenzhen 518055, China*

Meng Gu − *Department of Materials Science and Engineering, Southern University of Science and Technology, Shenzhen 518055, China;* orcid.org/0000-0002-5126-9611

Andrea E. Russell − *School of Chemistry, University of Southampton, Highfield, Southampton SO17 1BJ, U.K.;* orcid.org/0000-0002-8382-6443

Complete contact information is available at: https://pubs.acs.org/10.1021/acsami.1c19298

Author Contributions

The experiments were devised by M.J.L. and P.R. M.J.L. performed the synthesis and physical and electrochemical characterization of the materials. P.R. performed OLEMS characterization and analyses. E.S. conducted NMR characterization. M.J.L., V.C., P.R., L.S., and H.H. conducted the measurement of in situ XAS spectra. M.J.L. and V.C. performed XANES analysis and V.C. performed EXAFS fit analyses. Y.Z. and M.G. performed STEM HAADF-EDS. J.R.-L. provided guidance and discussions at different stages of this work. All authors contributed to the final preparation of the manuscript.

Notes

The authors declare no competing financial interest.

■ ACKNOWLEDGMENTS

We acknowledge the Diamond Light Source for provision of beamtime (SP21533). MJL acknowledges the University of Birmingham for financial support through Ph.D. scholarships at the School of Chemistry. P.R. acknowledges the University of Birmingham for financial support. E.S. acknowledges the University of Birmingham and the EPSRC Centre for Doctoral Training in Carbon Capture and Storage and Cleaner Fossil Energy for financial support through Ph.D. scholarships at the School of Chemistry. H.H. acknowledges fellowship support from the China Scholarship Council (201608440295) and the University of Southampton. M.G. and Y.Z. want to acknowledge the funding from the National Natural Science Foundation of China (No. 21802065, No. 12004156) and Shenzhen Natural Science Fund (Grant No. 20200925154115001 and JCYJ20190809181601639).

■ REFERENCES

(1) Olah, G. A.; Surya Prakash, G. K.; Goeppert, A. Anthropogenic Chemical Carbon Cycle for a Sustainable Future. *J. Am. Chem. Soc.* **2011**, *133*, 12881−12898.

(2) Alper, E.; Yuksel Orhan, O. CO2 Utilization: Developments in Conversion Processes. *Petroleum* **2017**, *3*, 109−126.

(3) Nielsen, D. U.; Hu, X.-M.; Daasbjerg, K.; Skrydstrup, T. Chemically and Electrochemically Catalysed Conversion of CO2 to CO with follow-up utilization to value-added Chemicals. *Nat. Catal.* **2018**, *1*, 244−254.

(4) Schreier, M.; Héroguel, F.; Steier, L.; Ahmad, S.; Luterbacher, J. S.; Mayer, M. T.; Luo, J.; Grätzel, M. Solar Conversion of CO2 to CO

using Earth-abundant Electrocatalysts prepared by Atomic Layer Modification of CuO. *Nat. Energy* **2017**, *2*, 17087.
(5) Seh, Z. W.; Kibsgaard, J.; Dickens, C. F.; Chorkendorff, I.; Nørskov, J. K.; Jaramillo, T. F. Combining Theory and Experiment in Electrocatalysis: Insights into Materials Design. *Science* **2017**, *355*, No. eaad4998.
(6) Montoya, J. H.; Seitz, L. C.; Chakthranont, P.; Vojvodic, A.; Jaramillo, T. F.; Norskov, J. K. Materials for Solar Fuels and Chemicals. *Nat. Mater.* **2016**, *16*, 70−81.
(7) Whipple, D. T.; Kenis, P. J. A. Prospects of CO2 Utilization via Direct Heterogeneous Electrochemical Reduction. *J. Phys. Chem. Lett.* **2010**, *1*, 3451−3458.
(8) Kuhl, K. P.; Cave, E. R.; Abram, D. N.; Jaramillo, T. F. New Insights into the Electrochemical Reduction of Carbon Dioxide on Metallic Copper Surfaces. *Energy Environ. Sci.* **2012**, *5*, 7050.
(9) Hori, Y.; Takahashi, I.; Koga, O.; Hoshi, N. Selective Formation of C2 Compounds from Electrochemical Reduction of CO2 at a Series of Copper Single Crystal Electrodes. *J. Phys. Chem. B* **2002**, *106*, 15−17.
(10) Takahashi, I.; Koga, O.; Hoshi, N.; Hori, Y. Electrochemical reduction of CO2 at copper single crystal Cu(S)-[n(111)×(111)] and Cu(S)-[n(110)×(100)] electrodes. *J. Electroanal. Chem.* **2002**, *533*, 135−143.
(11) Mistry, H.; Varela, A. S.; Bonifacio, C. S.; Zegkinoglou, I.; Sinev, I.; Choi, Y. W.; Kisslinger, K.; Stach, E. A.; Yang, J. C.; Strasser, P.; Cuenya, B. R. Highly Selective Plasma-activated Copper Catalysts for Carbon Dioxide Reduction to Ethylene. *Nat. Commun.* **2016**, *7*, 12123.
(12) Arán-Ais, R. M.; Scholten, F.; Kunze, S.; Rizo, R.; Roldan Cuenya, B. The Role of in situ generated Morphological Motifs and Cu(i) Species in C2+ Product Selectivity during CO2 Pulsed Electroreduction. *Nat. Energy* **2020**, *5*, 317−325.
(13) Grosse, P.; Gao, D.; Scholten, F.; Sinev, I.; Mistry, H.; Roldan Cuenya, B. Dynamic Changes in the Structure, Chemical State and Catalytic Selectivity of Cu Nanocubes during CO2 Electroreduction: Size and Support Effects. *Angew. Chem., Int. Ed.* **2018**, *57*, 6192−6197.
(14) Reske, R.; Mistry, H.; Behafarid, F.; Roldan Cuenya, B.; Strasser, P. Particle Size Effects in the Catalytic Electroreduction of CO(2) on Cu nanoparticles. *J. Am. Chem. Soc.* **2014**, *136*, 6978−6986.
(15) Kas, R.; Kortlever, R.; Milbrat, A.; Koper, M. T. M.; Mul, G.; Baltrusaitis, J. Electrochemical CO2 Reduction on Cu2O-derived Copper Nanoparticles: Controlling the Catalytic Selectivity of Hydrocarbons. *Phys. Chem. Chem. Phys.* **2014**, *16*, 12194−12201.
(16) De Luna, P.; Quintero-Bermudez, R.; Dinh, C.-T.; Ross, M. B.; Bushuyev, O. S.; Todorović, P.; Regier, T.; Kelley, S. O.; Yang, P.; Sargent, E. H. Catalyst Electro-redeposition Controls Morphology and Oxidation State for Selective Carbon Dioxide Reduction. *Nat. Catal.* **2018**, *1*, 103−110.
(17) Gao, D.; Sinev, I.; Scholten, F.; Arán-Ais, R. M.; Divins, N. J.; Kvashnina, K.; Timoshenko, J.; Roldan Cuenya, B. Selective CO2 Electroreduction to Ethylene and Multicarbon Alcohols via Electrolyte-Driven Nanostructuring. *Angew. Chem., Int. Ed.* **2019**, *58*, 17047−17053.
(18) Varela, A. S.; Kroschel, M.; Reier, T.; Strasser, P. Controlling the Selectivity of CO2 Electroreduction on Copper: The Effect of the Electrolyte Concentration and the importance of the Local pH. *Catal. Today* **2016**, *260*, 8−13.
(19) Colic, V.; Pohl, M. D.; Scieszka, D.; Bandarenka, A. S. Influence of the Electrolyte Composition on the Activity and Selectivity of Electrocatalytic Centers. *Catal. Today* **2016**, *262*, 24−35.
(20) Favaro, M.; Xiao, H.; Cheng, T.; Goddard, W. A., 3rd; Yano, J.; Crumlin, E. J. Subsurface Oxide plays a Critical Role in CO2 Activation by Cu(111) surfaces to form Chemisorbed CO2, the First Step in Reduction of CO2. *Proc. Natl. Acad. Sci. U. S. A.* **2017**, *114*, 6706−6711.
(21) Eilert, A.; Cavalca, F.; Roberts, F. S.; Osterwalder, J.; Liu, C.; Favaro, M.; Crumlin, E. J.; Ogasawara, H.; Friebel, D.; Pettersson, L. G.; Nilsson, A. Subsurface Oxygen in Oxide-Derived Copper Electrocatalysts for Carbon Dioxide Reduction. *J. Phys. Chem. Lett.* **2017**, *8*, 285−290.
(22) le Duff, C. S.; Lawrence, M. J.; Rodriguez, P. Role of the Adsorbed Oxygen Species in the Selective Electrochemical Reduction of CO2 to Alcohols and Carbonyls on Copper Electrodes. *Angew. Chem., Int. Ed.* **2017**, *56*, 12919−12924.
(23) Garza, A. J.; Bell, A. T.; Head-Gordon, M. Is Subsurface Oxygen Necessary for the Electrochemical Reduction of CO2 on Copper? *J. Phys. Chem. Lett.* **2018**, *9*, 601−606.
(24) Scott, S. B.; Hogg, T. V.; Landers, A. T.; Maagaard, T.; Bertheussen, E.; Lin, J. C.; Davis, R. C.; Beeman, J. W.; Higgins, D.; Drisdell, W. S.; Hahn, C.; Mehta, A.; Seger, B.; Jaramillo, T. F.; Chorkendorff, I. Absence of Oxidized Phases in Cu under CO Reduction Conditions. *ACS Energy Lett.* **2019**, *4*, 803−804.
(25) Cueto, L. F.; Hirata, G. A.; Sánchez, E. M. Thin-film TiO2 Electrode Surface Characterization upon CO2 Reduction Processes. *J. Sol-Gel Sci. Technol.* **2006**, *37*, 105−109.
(26) Lawrence, M. J.; Celorrio, V.; Shi, X. B.; Wang, Q.; Yanson, A.; Adkins, N. J. E.; Gu, M.; Rodríguez-López, J.; Rodriguez, P. Electrochemical Synthesis of Nanostructured Metal-Doped Titanates and Investigation of Their Activity as Oxygen Evolution Photoanodes. *ACS Appl. Energy Mater.* **2018**, *1*, 5233−5244.
(27) Kromer, M. L.; Monzó, J.; Lawrence, M. J.; Kolodziej, A.; Gossage, Z. T.; Simpson, B. H.; Morandi, S.; Yanson, A.; Rodríguez-López, J.; Rodríguez, P. High-Throughput Preparation of Metal Oxide Nanocrystals by Cathodic Corrosion and Their Use as Active Photocatalysts. *Langmuir* **2017**, *33*, 13295−13302.
(28) Lawrence, M. J.; Kolodziej, A.; Rodriguez, P. Controllable Synthesis of Nanostructured Metal Oxide and Oxyhydroxide Materials via Electrochemical Methods. *Curr. Opin. Electrochem.* **2018**, *10*, 7−15.
(29) Yanson, A. I.; Rodriguez, P.; Garcia-Araez, N.; Mom, R. V.; Tichelaar, F. D.; Koper, M. T. M. Cathodic Corrosion: a Quick, Clean, and Versatile Method for the Synthesis of Metallic Nanoparticles. *Angew. Chem., Int. Ed.* **2011**, *50*, 6346−6350.
(30) Rodriguez, P.; Tichelaar, F. D.; Koper, M. T. M.; Yanson, A. I. Cathodic Corrosion as a Facile and Effective Method to prepare Clean Metal Alloy Nanoparticles. *J. Am. Chem. Soc.* **2011**, *133*, 17626−17629.
(31) García-Cañadas, J.; Adkins, N. J.; McCain, S.; Hauptstein, B.; Brew, A.; Jarvis, D. J.; Min, G. Accelerated Discovery of Thermoelectric Materials: Combinatorial Facility and High-Throughput Measurement of Thermoelectric Power Factor. *ACS Comb. Sci.* **2016**, *18*, 314−319.
(32) Li, S.; Adkins, N. J. E.; McCain, S.; Attallah, M. M. Suspended Droplet Alloying: A new method for Combinatorial Alloy Synthesis; Nitinol-based Alloys as an example. *J. Alloys Compd.* **2018**, *768*, 392−398.
(33) Binninger, T.; Pribyl, B.; Pătru, A.; Ruettimann, P.; Bjelić, S.; Schmidt, T. J. Multivariate Calibration Method for Mass Spectrometry of Interfering Gases such as Mixtures of CO, N2 , and CO2. *J. Mass Spectrom.* **2018**, *53*, 1214−1221.
(34) Dent, A. J.; Cibin, G.; Ramos, S.; Smith, A. D.; Scott, S. M.; Varandas, L.; Pearson, M. R.; Krumpa, N. A.; Jones, C. P.; Robbins, P. E. B18: A Core XAS Spectroscopy Beamline for Diamond. *J. Phys.: Conf. Ser.* **2009**, *190*, No. 012039.
(35) Wise, A. M.; Richardson, P. W.; Price, S. W. T.; Chouchelamane, G.; Calvillo, L.; Hendra, P. J.; Toney, M. F.; Russell, A. E. Inhibitive effect of Pt on Pd-hydride Formation of Pd@Pt core-shell Electrocatalysts: An in situ EXAFS and XRD study. *Electrochim. Acta* **2018**, *262*, 27−38.
(36) Newville, M. EXAFS analysis using FEFF and FEFFIT. *J. Synchrotron Radiat.* **2001**, *8*, 96−100.
(37) Ota, M.; Hirota, Y.; Uchida, Y.; Sakamoto, Y.; Nishiyama, N. Low Temperature Synthesized H2Ti3O7 Nanotubes with a High CO2 Adsorption Property by Amine Modification. *Langmuir* **2018**, *34*, 6814−6819.
(38) Sharma, A.; Varshney, M.; Park, J.; Ha, T.-K.; Chae, K.-H.; Shin, H.-J. XANES, EXAFS and Photocatalytic Investigations on Copper Oxide Nanoparticles and Nanocomposites. *RSC Adv.* **2015**, *5*, 21762−21771.
(39) Gaur, A.; Shrivastava, B. D. A Comparative Study of the Methods of Speciation Using X-ray Absorption Fine Structure. *Acta Phys. Pol., A* **2012**, *121*, 647−652.

https://doi.org/10.1021/acsami.1c19298
ACS Appl. Mater. Interfaces 2022, 14, 2742−2753

(40) Imbao, J.; van Bokhoven, J. A.; Clark, A.; Nachtegaal, M. Elucidating the Mechanism of Heterogeneous Wacker Oxidation over Pd-Cu/zeolite Y by transient XAS. *Nat. Commun.* **2020**, *11*, 1118.
(41) Gaur, A.; Shrivastava, B. D.; Joshi, S. K. Copper K-edge XANES of Cu(I) and Cu(II) Oxide Mixtures. *J. Phys.: Conf. Ser.* **2009**, *190*, No. 012084.
(42) Pelliccione, C. J.; Li, Y. R.; Marschilok, A. C.; Takeuchi, K. J.; Takeuchi, E. S. X-ray Absorption Spectroscopy of Lithium Insertion and De-insertion in Copper Birnessite Nanoparticle Electrodes. *Phys. Chem. Chem. Phys.* **2016**, *18*, 2959−2967.
(43) Li, J.; Che, F.; Pang, Y.; Zou, C.; Howe, J. Y.; Burdyny, T.; Edwards, J. P.; Wang, Y.; Li, F.; Wang, Z.; De Luna, P.; Dinh, C. T.; Zhuang, T. T.; Saidaminov, M. I.; Cheng, S.; Wu, T.; Finfrock, Y. Z.; Ma, L.; Hsieh, S. H.; Liu, Y. S.; Botton, G. A.; Pong, W. F.; Du, X.; Guo, J.; Sham, T. K.; Sargent, E. H.; Sinton, D. Copper Adparticle enabled Selective Electrosynthesis of n-propanol. *Nat. Commun.* **2018**, *9*, 4614.
(44) Lee, S. H.; Sullivan, I.; Larson, D. M.; Liu, G.; Toma, F. M.; Xiang, C.; Drisdell, W. S. Correlating Oxidation State and Surface Area to Activity from Operando Studies of Copper CO Electroreduction Catalysts in a Gas-Fed Device. *ACS Catal.* **2020**, *10*, 8000−8011.
(45) Fabregat-Santiago, F.; Mora-Seró, I.; Garcia-Belmonte, G.; Bisquert, J. Cyclic Voltammetry Studies of Nanoporous Semiconductors. Capacitive and Reactive Properties of Nanocrystalline TiO2 Electrodes in Aqueous Electrolyte. *J. Phys. Chem. B* **2003**, *107*, 758−768.
(46) Gao, D.; Arán-Ais, R. M.; Jeon, H. S.; Roldan Cuenya, B. Rational Catalyst and Electrolyte Design for CO2 Electroreduction towards Multicarbon Products. *Nat. Catal.* **2019**, *2*, 198−210.
(47) Li, C. W.; Ciston, J.; Kanan, M. W. Electroreduction of Carbon Monoxide to Liquid Fuel on Oxide-derived Nanocrystalline Copper. *Nature* **2014**, *508*, 504−507.
(48) Li, C. W.; Kanan, M. W. CO2 Reduction at Low Overpotential on Cu Electrodes Resulting from the Reduction of Thick Cu2O Films. *J. Am. Chem. Soc.* **2012**, *134*, 7231−7234.
(49) Monzó, J.; Malewski, Y.; Kortlever, R.; Vidal-Iglesias, F. J.; Solla-Gullón, J.; Koper, M. T. M.; Rodriguez, P. Enhanced Electrocatalytic Activity of Au@Cu core@shell Nanoparticles towards CO2 Reduction. *J. Mater. Chem. A* **2015**, *3*, 23690−23698.
(50) Morales-Guio, C. G.; Cave, E. R.; Nitopi, S. A.; Feaster, J. T.; Wang, L.; Kuhl, K. P.; Jackson, A.; Johnson, N. C.; Abram, D. N.; Hatsukade, T.; Hahn, C.; Jaramillo, T. F. Improved CO2 Reduction Activity towards C2+ Alcohols on a tandem Gold on Copper Electrocatalyst. *Nat. Catal.* **2018**, *1*, 764−771.
(51) Herzog, A.; Bergmann, A.; Jeon, H. S.; Timoshenko, J.; Kühl, S.; Rettenmaier, C.; Lopez Luna, M.; Haase, F. T.; Roldan Cuenya, B. Operando Investigation of Ag-Decorated Cu2O Nanocube Catalysts with Enhanced CO2 Electroreduction toward Liquid Products. *Angew. Chem., Int. Ed.* **2021**, *60*, 7426−7435.
(52) Velasco-Velez, J.-J.; Mom, R. V.; Sandoval-Diaz, L.-E.; Falling, L. J.; Chuang, C.-H.; Gao, D.; Jones, T. E.; Zhu, Q.; Arrigo, R.; Roldan Cuenya, B.; Knop-Gericke, A.; Lunkenbein, T.; Schlögl, R. Revealing the Active Phase of Copper during the Electroreduction of CO2 in Aqueous Electrolyte by Correlating In Situ X-ray Spectroscopy and In Situ Electron Microscopy. *ACS Energy Lett.* **2020**, *5*, 2106−2111.
(53) Gao, D.; Zegkinoglou, I.; Divins, N. J.; Scholten, F.; Sinev, I.; Grosse, P.; Roldan Cuenya, B. Plasma-Activated Copper Nanocube Catalysts for Efficient Carbon Dioxide Electroreduction to Hydrocarbons and Alcohols. *ACS Nano* **2017**, *11*, 4825−4831.
(54) Zhang, Y. J.; Peterson, A. A. Oxygen-induced changes to Selectivity-determining steps in Electrocatalytic CO2 Reduction. *Phys. Chem. Chem. Phys.* **2015**, *17*, 4505−4515.
(55) Xiao, H.; Goddard, W. A., 3rd; Cheng, T.; Liu, Y. Cu Metal Embedded in Oxidized Matrix Catalyst to Promote CO2 Activation and CO Dimerization for Electrochemical Reduction of CO2. *Proc. Natl. Acad. Sci. U. S. A.* **2017**, *114*, 6685−6688.
(56) Zhou, Y.; Che, F.; Liu, M.; Zou, C.; Liang, Z.; De Luna, P.; Yuan, H.; Li, J.; Wang, Z.; Xie, H.; Li, H.; Chen, P.; Bladt, E.; Quintero-Bermudez, R.; Sham, T. K.; Bals, S.; Hofkens, J.; Sinton, D.; Chen, G.; Sargent, E. H. Dopant-induced Electron Localization drives CO2 Reduction to C2 Hydrocarbons. *Nat. Chem.* **2018**, *10*, 974−980.
(57) Dong, W. J.; Yoo, C. J.; Lim, J. W.; Park, J. Y.; Kim, K.; Kim, S.; Lee, D.; Lee, J.-L. Tailoring electronic structure of bifunctional Cu/Ag layered electrocatalysts for selective CO2 reduction to CO and CH4. *Nano Energy* **2020**, *78*, No. 105168.
(58) Dong, W. J.; Lim, J. W.; Hong, D. M.; Kim, J.; Park, J. Y.; Cho, W. S.; Baek, S.; Lee, J. L. Grain Boundary Engineering of Cu-Ag Thin-Film Catalysts for Selective (Photo)Electrochemical CO2 Reduction to CO and CH4. *ACS Appl. Mater. Interfaces* **2021**, *13*, 18905−18913.
(59) Gao, D.; Zhang, Y.; Zhou, Z.; Cai, F.; Zhao, X.; Huang, W.; Li, Y.; Zhu, J.; Liu, P.; Yang, F.; Wang, G.; Bao, X. Enhancing CO2 Electroreduction with the Metal-Oxide Interface. *J. Am. Chem. Soc.* **2017**, *139*, 5652−5655.
(60) Chen, C. S.; Handoko, A. D.; Wan, J. H.; Ma, L.; Ren, D.; Yeo, B. S. Stable and Selective Electrochemical Reduction of Carbon Dioxide to Ethylene on Copper Mesocrystals. *Catal. Sci. Technol.* **2015**, *5*, 161−168.
(61) Roberts, F. S.; Kuhl, K. P.; Nilsson, A. High Selectivity for Ethylene from Carbon Dioxide Reduction over Copper Nanocube Electrocatalysts. *Angew. Chem., Int. Ed.* **2015**, *54*, 5179−5182.
(62) Loiudice, A.; Lobaccaro, P.; Kamali, E. A.; Thao, T.; Huang, B. H.; Ager, J. W.; Buonsanti, R. Tailoring Copper Nanocrystals towards C2 Products in Electrochemical CO2 Reduction. *Angew. Chem., Int. Ed.* **2016**, *55*, 5789−5792.

https://doi.org/10.1021/acsami.1c19298
ACS Appl. Mater. Interfaces 2022, 14, 2742−2753